Journal of Materials Chemistry A

ROYAL SOCIETY OF CHEMISTRY

PAPER

View Article Online
View Journal

Cite this: DOI: 10.1039/d6ta00222f

Accelerated synthesis of titanium-Beta zeolites using *N*-methyl-2-pyrrolidone and Beta seeds

Hedieh Tabatabaeizadeh, [a] Francesca Rosso, [a] Francesca Bonino, [a] Silvia Bordiga, [a] Valentina Crocellà, [a] Miguel A. Camblor [b] and Matteo Signorile *[a]

The accelerated synthesis of titanium-Beta (Ti-Beta) zeolites is essential for improving their scalability and catalytic applicability. Here, we report a rapid hydrothermal route for the synthesis of Ti-Beta by combining *N*-methyl-2-pyrrolidone (NMP) as a crystallization accelerator with seed-assisted growth. It is proposed that NMP can accelerate the crystallisation by increasing the TEA^+ concentration during the synthesis by preventing the Hofmann degradation of TEAOH at high temperatures. Using this optimized strategy, highly crystalline Ti-Beta is obtained in just 20 hours, approximately 20 times faster than conventional syntheses under otherwise identical conditions. Spectroscopic analyses confirm that the synergy of NMP and seeds enhances nucleation and crystallization kinetics while maintaining high incorporation of framework Ti species. UV-vis spectra showing the characteristic 210–220 nm charge-transfer band of tetrahedral Ti(IV) and additional features upon H_2O_2 interaction support the formation of catalytically relevant Ti-peroxo species. Raman spectroscopy rules out the presence of extra-framework TiO_2, SEM imaging reveals reduced crystal size in seeded samples, and N_2 physisorption confirms preservation of microporosity. Acid site accessibility, assessed by *in situ* IR spectroscopy using acetonitrile as a probe, provided direct evidence of the Lewis acidic behaviour of framework Ti sites. Overall, this work demonstrates how the combined use of organic accelerators and seeding synergistically tailors the crystallization pathway, enabling rapid production of high-quality Ti-Beta zeolites.

Received 8th January 2026
Accepted 11th March 2026

DOI: 10.1039/d6ta00222f

rsc.li/materials-a

Introduction

Ti-substituted zeolites have attracted considerable attention as environmentally friendly heterogeneous catalysts for selective oxidation reactions using hydrogen peroxide as a green oxidant. Among these, TS-1 (with MFI topology) has been widely studied due to its well-defined framework-incorporated Ti sites and excellent activity in epoxidation and hydroxylation reactions.[1–3] However, the medium pore size of TS-1 restricts its application to small substrates (*e.g.* propylene). In contrast, the Beta zeolite framework, composed of a three-dimensional network of large 12-membered-ring channels, offers larger pore dimensions, making Ti-substituted Beta (Ti-Beta) a promising candidate for the oxidation of larger molecules such as cyclohexene and long-chain olefins.[2,4]

Despite its potential, the synthesis of Ti-Beta remains challenging. Conventional hydrothermal methods often require prolonged crystallization times over a week to yield a well-crystallized product.[5] Moreover, ensuring effective incorporation of Ti into the silica framework is nontrivial, as titanium alkoxides are prone to rapid hydrolysis and can lead to the formation of extra-framework Ti species or even crystalline TiO_2 (anatase), both of which are catalytically inactive. Strategies such as fluoride-mediated synthesis and seed-assisted crystallization have been developed to overcome these limitations by enhancing phase selectivity and promoting nucleation.[6] However, achieving fast crystallization while maintaining high-quality framework Ti incorporation remains a key obstacle.[7–15]

The use of *N*-methyl-2-pyrrolidone (NMP) as an additive in zeolite synthesis has recently attracted attention due to its unusual, temperature-dependent functionality.[16,17] At relatively low crystallization temperatures (120–140 °C), NMP acts as a crystallization promoter,[18,19] accelerating nucleation of Beta zeolites by maintaining the concentration of TEA^+, the structure-directing agent (SDA), through decreasing its Hofman degradation, thereby enabling rapid crystallization of Beta zeolites (Scheme 1). In this way, NMP indirectly promotes crystallization by preserving favourable gel chemistry and enabling efficient nucleation and growth. At higher temperatures (~160 °C), NMP instead plays the role of a hollow-directing agent,[18] resulting in hollow-box Beta morphologies. However, at even higher synthesis temperatures (≥180 °C), the

[a]Department of Chemistry, NIS Centre, INSTM Research Unit, Università di Torino, Via G. Quarello 15/A and Via P. Giuria 7, Turin 10135, Italy. E-mail: matteo.signorile@unito.it

[b]Instituto de Ciencia de Materiales de Madrid, Consejo Superior de Investigaciones Científicas (ICMM-CSIC), c/Sor Juana Inés de la Cruz 3, 28049, Madrid, Spain

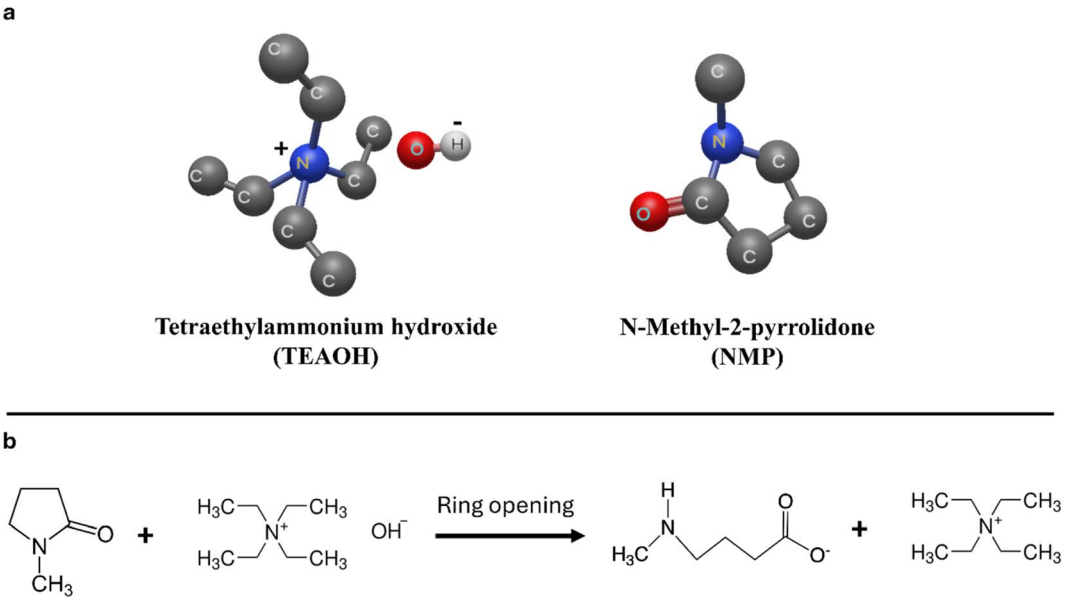

Scheme 1 Illustration of (a) the chemical structures of TEAOH and NMP, and (b) alkali-catalyzed ring opening product of NMP.

acceleration effect of NMP is reduced due to the decomposition of TEAOH through Hofmann degradation, decreasing the effective concentration of TEA^+ cations in solution and thus suppressing Beta crystallization in favour of competing phases such as ZSM-5 and ZSM-12.[18–21] Importantly, spectroscopic analyses confirm that NMP is not occluded within the zeolite framework, but rather functions indirectly by modifying the solution chemistry and SDA stability.[18–21] Notably, NMP has been used to accelerate the crystallization of Al-substituted Beta zeolites;[20] however, its role in the crystallization of heteroatom-substituted zeolites, particularly Ti-containing Beta, has not been explored yet.

In this work, we present a one-pot strategy for the accelerated crystallization of Ti-Beta zeolites using NMP and dealuminated Beta seeds. Since the role of NMP is strongly temperature-dependent, this study intentionally focused on synthesis at 140 °C, which is the typical temperature for obtaining the conventional non-hollow Beta framework. Furthermore, the basic synthesis parameters were maintained constant to ensure that the observed phase and morphological transitions could be attributed primarily to the crystallization time, and addition of NMP, dealuminated Beta seeds or HF.

Experimental section

Chemicals

All chemicals were used as received without further purification. Fumed silica 380 (Sigma-Aldrich), sodium hydroxide (NaOH, Merck), aluminium sulfate 18-hydrate pure ($Al_2(SO_4)_3$–$18H_2O$, PanReacAppliChem, ITW reagents), sodium aluminate anhydrous ($NaAlO_2$, 56 wt% Al_2O_3 and 44 wt% Na_2O, Riedel-de Haen), tetraethyl orthosilicate (TEOS, Sigma-Aldrich, 98%), tetraethyl orthotitanate (TEOT, Aldrich), tetraethylammonium hydroxide (TEAOH, Aldrich, 35 wt% in water), hydrogen peroxide (H_2O_2, Fisher, 30 wt% in water), *N*-methyl-2-pyrrolidone (NMP, Sigma-Aldrich, ≥99%), hydrofluoric acid (HF, Labkem, 40% aqueous solution), nitric acid (HNO_3, Sigma-Aldrich, 70%) and ammonium nitrate (NH_4NO_3, Sigma-Aldrich) were obtained. Ethanol and Milli-Q water (resistivity ≥ 18.2 MΩ cm) were used in all syntheses.

Synthesis procedure of Al-Beta zeolites

Zeolite Beta was hydrothermally synthesized following the approach described in the literature with some modifications.

The starting gel was prepared with the molar composition:

3.00 NMP : 1.00 SiO_2 : 0.04 Al_2O_3 : 0.056 Na_2O : 0.64 TEAOH : 15.84 H_2O

In a typical synthesis as adapted from ref. 20, 0.27 g of $NaAlO_2$, 0.09 g of NaOH, 0.52 g of $Al_2(SO_4)_3$, 13.06 mL of TEAOH and 3 mL of deionized water were successively added in a PET bottle at room temperature under vigorous stirring for 2 h, till the aluminium precursor fully hydrolyses and a clear solution is obtained. Subsequently, 13.06 mL of NMP, 3.33 g of fumed silica 380 and 2.4 mL of deionized water were added in sequence. Finally, after stirring for 3 h, the resulting gel was transferred to a 45 mL Teflon-lined stainless-steel autoclave and heated at 140 °C in an oven while tumbling at 52 rpm rotation for 24 h. The sample was carefully recovered *via* centrifugation at 10 000 rpm for 10 min, washed with Milli-Q water and ethanol and finally dried overnight at 85 °C. The dry powder was eventually calcined at 550 °C for 6 h, at a heating rate of 3 °C min^{-1} in air in a muffle oven.

Preparation of dealuminated Beta-seeds

The Na^+, H^+–Beta zeolite obtained as described above was ion-exchanged to ammonium form with 100 mL 1.0 M NH_4NO_3 solution per 2.0 g of Na-Beta zeolite at 80 °C for 24 h to exchange

Na^+ and H^+ with NH_4^+. The final product was washed with Milli-Q water, dried at 65 °C and calcined under the aforementioned conditions. For the dealumination process, 1.5 g of the NH_4^+–Beta powder was added to 30 mL of 13 M HNO_3 solution in a conical flask under vigorous stirring at room temperature for 24 h.[22] The final product was washed with Milli-Q water until the pH became neutral. Finally, the powder was dried at 65 °C and calcined under the same conditions as before.

Synthesis procedure of Ti-Beta zeolites

In a typical synthesis, gel composition used as the starting point was:

X NMP : 0.017 TiO_2 : 1 SiO_2 : 0.55 TEAOH : *Y* HF : 0.33 H_2O_2 : 7.625 H_2O : *Z* seed.

The synthesis procedure follows:[23] 3.74 g of TEOS was added to 4.10 g of TEAOH in a PET bottle and stirred vigorously at room temperature. In the case of using the accelerator, 5.17 mL of NMP (corresponding to a NMP/SiO_2 ratio of $X = 3$) was introduced, (in different experiments, NMP was added at different times). The resulting mixture was stirred continuously for 3 h to ensure complete hydrolysis of the silica source. To facilitate the hydrolysis of the titanium precursor, 0.69 g of H_2O_2 was added prior to the dropwise addition of 0.06 mL of TEOT under an inert atmosphere (*i.e.*, N_2), due to its sensitivity to moisture and air. The mixture was stirred overnight to promote homogeneity. Next, if required by the specific procedure, 0.06 g of dealuminated Beta zeolite seeds (prepared as described in the previous section, and corresponding to a seed/SiO_2 ratio of $Z = 0.05$, considering them as pure SiO_2 for the purpose of gel molar composition calculation) were added. After ethanol evaporation and adjusting the water content to the target value, 0.43 mL of HF (corresponding to a HF/SiO_2 ratio of $Y = 0.55$) was added as the final component when applicable (caution: HF must be handled exclusively in a fume hood using appropriate personal protective equipment due to its corrosive and toxic nature). The final gel was transferred into a 45 mL Teflon-lined stainless-steel autoclave and subjected to crystallization under tumbling conditions (52 rpm and 140 °C) for *x* hours, depending on the experimental matrix (Table 1). The resulting solids were recovered by centrifugation at 10 000 rpm for 10 min, washed thoroughly with Milli-Q water and ethanol, and dried overnight at 80 °C. The dried samples were subsequently calcined in air at 550 °C for 6 h (heating rate: 3 °C min^{-1}) to remove the organic residuals.

The details of all syntheses performed in this work are mentioned in Table 1 along with the corresponding sample code. In the mentioned codes, the letters N, S, and F are shortened for the use of NMP, seed, and HF in the synthesis. All the characterization experiments in this study were performed on the calcined samples.

Characterization methods

The calcined samples listed in Table 1 were characterized by using a combination of structural, spectroscopic, and textural techniques in order to evaluate crystallinity, Ti incorporation, and porosity. Powder X-ray diffraction (XRD) patterns were recorded on a PANalytical X'Pert diffractometer (Bragg–Brentano geometry) using Cu Kα radiation ($\lambda = 1.5418$ Å) and a X'Celerator strip detector. Patterns were collected in the 2θ range of 3–45° with a step size of 0.02° and a counting time of 50 s per step.

The speciation of Ti species was assessed using UV-vis spectroscopy in Diffuse Reflectance (DR) mode and Fourier Transform (FT) IR spectroscopy in Attenuated Total Reflectance (ATR) mode. DR-UV-vis spectra were collected on a Varian Cary5000 spectrophotometer, equipped with a DR sphere, on the pure samples (Spectralon® was used as the 100% reflectance reference). ATR-IR spectra were recorded on a Bruker Alpha II FTIR spectrometer located inside a N_2-filled glovebox. The spectra were recorded with a DTGS detector by averaging 64 scans (128 for the background spectrum). All the samples were measured as such and after the following activation procedure, aiming to eliminate the influence of water and possible organic pollutants on the Ti coordination environment: the samples were heated to 500 °C at a ramp rate of 5 °C min^{-1} under dynamic vacuum, outgassed for 1 h at 500 °C (residual pressure $< 10^{-3}$ mbar) and then exposed to 100 mbar of pure oxygen (for 30 min); eventually, the samples were further outgassed for 1 h prior to cooling. After the activation, the samples were transferred from the activation cell to the IR spectrophotometer to collect ATR spectra or to sealed UV-vis cells inside a N_2-filled glovebox ($H_2O < 0.5$ ppm), in order to avoid any rehydration or contamination.

N_2 physisorption measurements were carried out at −196 °C using a Micromeritics 3Flex instrument. The samples were degassed under vacuum at 400 °C for 4 h prior to analysis. The surface area was calculated by applying the BET equation in the range of 0.008–0.040 p/p_0 (by fulfilling the Rouquerol criteria)[10,24] and the Langmuir model in the 8–18 kPa pressure range. Pore volume and pore size distribution were estimated with the DFT method, using the Tarazona NL-DFT model for a cylindrical pore geometry,[25,26] and using both the adsorption and desorption branches of the isotherm. The micropore surface area ($S_{micropore}$) and the external surface area ($S_{external}$) were determined by t-plot analysis of the N_2 adsorption isotherms, using the Harkins–Jura thickness equation. The linear region of the *t*-plot was selected in the statistical thickness range of 2.4–3.4 Å, and the BET surface area was used as a reference for the calculation.

The total Ti content (defined as "Ti/Si molar ratio and TiO_2 wt%") was determined using an energy dispersive X-ray, EDX detector (Oxford-Detector with an AZTEC software) while performing imaging with a Field Emission Scanning Electron Microscope, FESEM (Tescan S9000G with a Schottky FEG source).

Raman spectra were recorded using a Renishaw inVia Raman microscope equipped with a 785 nm excitation laser, operating in backscattering geometry. A 50× objective lens was used to focus the beam on the powdered samples, with the laser power limited to less than 1 mW at the sample to prevent undesired thermal effects. The spectral range 100–1500 cm^{-1} was collected, averaging 10 scans with an integration time of 30 s.

Table 1 Synthesis procedure of different samples

N	Code	Gel composition	Time (h)	Phase
1	Beta-N-24h	3.00 NMP : 1.00 SiO_2 : 0.04 Al_2O_3 : 0.056 Na_2O : 0.64 TEAOH : 15.84 H_2O	24	Beta
2	Ti-Beta-F-336h	0.017 TiO_2 : 1.00 SiO_2 : 0.55 TEAOH : 0.55 HF : 0.33 H_2O_2 : 7.625 H_2O	336	Beta
3	Ti-Beta-F-72h	0.017 TiO_2 : 1.00 SiO_2 : 0.55 TEAOH : 0.55 HF : 0.33 H_2O_2 : 7.625 H_2O	72	Amorphous
4	Ti-Beta-N-F-72h	3.00 NMP : 0.017 TiO_2 : 1.00 SiO_2 : 0.55 TEAOH : 0.55 HF : 0.33 H_2O_2 : 7.625 H_2O	72	Beta
5	Ti-Beta-N-S-F-72h	3.00 NMP : 0.017 TiO_2 : 1.00 SiO_2 : 0.55 TEAOH : 0.55 HF : 0.33 H_2O_2 : 7.625 H_2O : 0.05 seed	72	Beta
6	Ti-Beta-N-S-72h	3.00 NMP : 0.017 TiO_2 : 1.00 SiO_2 : 0.55 TEAOH : 0.33 H_2O_2 : 7.625 H_2O : 0.05 seed	72	Amorphous
7	Ti-Beta-N-S-F-48h	3.00 NMP : 0.017 TiO_2 : 1.00 SiO_2 : 0.55 TEAOH : 0.55 HF : 0.33 H_2O_2 : 7.625 H_2O : 0.05 seed	48	Beta
8	Ti-Beta-S-F-48h	0.017 TiO_2 : 1.00 SiO_2 : 0.55 TEAOH : 0.55 HF : 0.33 H_2O_2 : 7.625 H_2O : 0.05 seed	48	Amorphous
9	Ti-Beta-N-F-20h	3.00 NMP : 0.017 TiO_2 : 1.00 SiO_2 : 0.55 TEAOH : 0.55 HF : 0.33 H_2O_2 : 7.625 H_2O	20	Amorphous
10	Ti-Beta-N-S-F-20h	3.00 NMP : 0.017 TiO_2 : 1.00 SiO_2 : 0.55 TEAOH : 0.55 HF : 0.33 H_2O_2 : 7.625 H_2O : 0.05 seed	20	Beta
11	Ti-Beta-N-S-F-14h	3.00 NMP : 0.017 TiO_2 : 1.00 SiO_2 : 0.55 TEAOH : 0.55 HF : 0.33 H_2O_2 : 7.625 H_2O : 0.05 seed	14	Beta/Amorphous
12	Ti-Beta-N-S-F-6h	3.00 NMP : 0.017 TiO_2 : 1.00 SiO_2 : 0.55 TEAOH : 0.55 HF : 0.33 H_2O_2 : 7.625 H_2O : 0.05 seed	6	Amorphous

Order of the addition of NMP

N	Code	NMP addition	Gel composition	Time (h)	Phase
4a	Ti-Beta-N-F-72h-1	Before TEOT	3.00 NMP : 0.017 TiO_2 : 1 SiO_2 : 0.55 TEAOH : 0.55 HF : 0.33 H_2O_2 : 7.625 H_2O	72	Beta
4b	Ti-Beta-N-F-72h-2	After TEOT	3.00 NMP : 0.017 TiO_2 : 1 SiO_2 : 0.55 TEAOH : 0.55 HF : 0.33 H_2O_2 : 7.625 H_2O	72	Beta
4c	Ti-Beta-N-F-72h-3	Before HF	3.00 NMP : 0.017 TiO_2 : 1 SiO_2 : 0.55 TEAOH : 0.55 HF : 0.33 H_2O_2 : 7.625 H_2O	72	Amorphous

Thermogravimetric analysis (TGA) was carried out using a TA Instruments Q500 V20.13 Build 39. Approximately 5.8 mg of the sample was heated from room temperature to 800 °C at a rate of 10 °C min^{-1} under a nitrogen flow (balance gas: 40 mL min^{-1}; sample gas: 60 mL min^{-1}, nitrogen) using an alumina pan. Mass loss was continuously recorded as a function of temperature.

Results and discussion

The XRD patterns of Ti-Beta zeolites synthesized under various conditions are shown in Fig. 1. The diffraction pattern of the crystalline samples clearly exhibits the characteristic reflections of the Beta zeolite, with prominent peaks at $2\theta \approx 7.6°$, 21.5°, 22.5°, 25.3°, 27.0°, and 29.6°, which correspond to the (101),

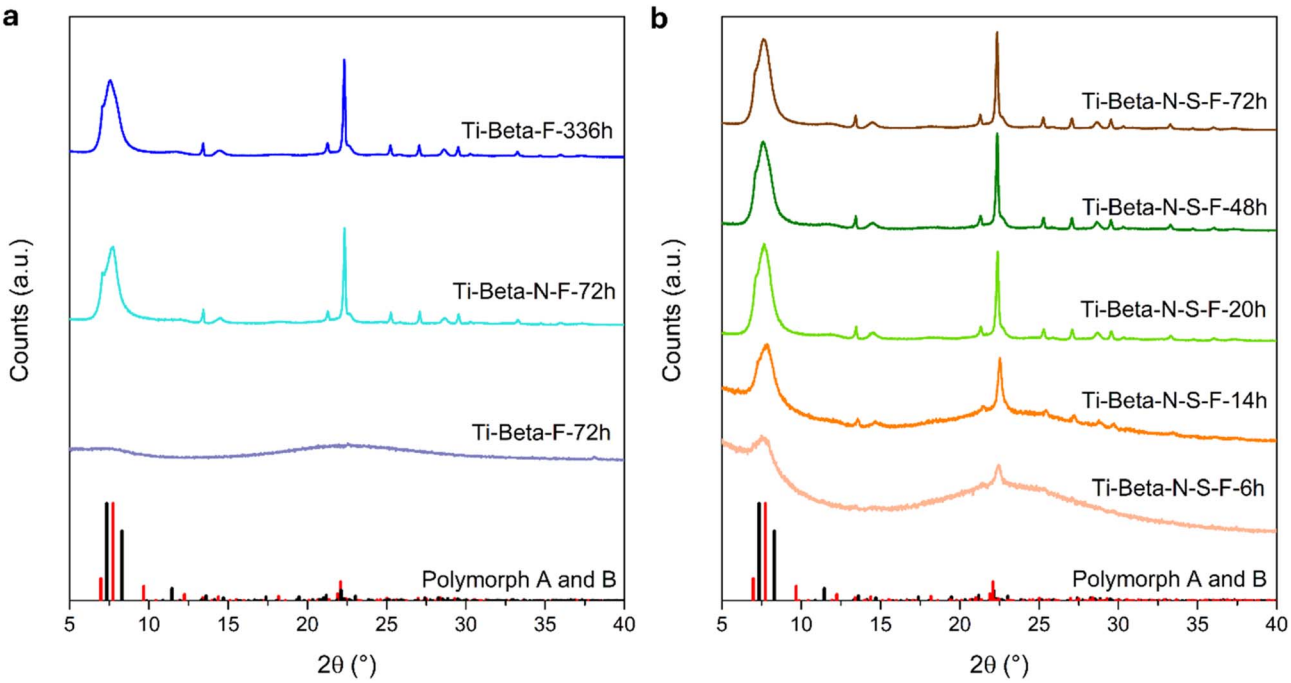

Fig. 1 XRD patterns of calcined samples synthesized under different conditions: (a) without using seeds and (b) using seeds. The diffractograms are normalized to their maximum intensity and vertically shifted for visual clarity. Simulated XRD pattern of Beta zeolites (polymorph A in red and polymorph B in black) based on the IZA database.[25]

(302), (303), (501), (303), and (060) reflections, respectively, taking polymorph A as a reference.[25] Furthermore, the presence of other zeolitic phases or bulk anatase in detectable amounts is excluded.[11,26]

As shown in Fig. 1, the crystallization of Ti-Beta in a fluoride medium requires 336 h[23] (Ti-Beta-F-336h). The presence of NMP markedly promotes crystallization, leading to the formation of crystalline Ti-Beta after only 72 h (Ti-Beta-N-F-72h). Without NMP, the same crystallization time leads to a completely amorphous material (Ti-Beta-F-72h). When seeds are introduced, a comparable degree of crystallinity is achieved after just 20 h (Ti-Beta-N-S-F-20h) and the crystallization has already started after 6 h (Ti-Beta-N-S-F-6h), though a large amorphous fraction is still observed. This indicates that seeding further accelerates the crystallization process by providing nucleation sites from the very early stages of synthesis. The crystallization in a fluoride medium in the presence of both NMP and seeds was further prolonged up to 72 h (Ti-Beta-N-S-F-48h and Ti-Beta-N-S-F-72h), showing that no different zeolitic phases nucleated. The relative crystallinity of the Ti-Beta-N-S-F series was determined from XRD data by summing the integration of the characteristic Beta reflections at approximately 7.5° and 22.5° (2θ). The Ti-Beta-N-S-F-48 h sample, which exhibits fully developed diffraction peaks, was defined as the 100% crystallinity reference. The other samples were normalized accordingly, yielding the following relative crystallinities: 6 h (amorphous, 0%), 14 h (20%), 20 h (95%), 48 h (100%), and 72 h (98%). Moreover, syntheses in the presence of only (i) NMP and seeds (Ti-Beta-N-S-72h), (ii) seeds and fluoride (Ti-Beta-S-F-48h) and (iii) NMP and fluoride (Ti-Beta-N-F-72h) were conducted to determine the importance of the three factors in the intermediate crystallization time (Fig. S1 of the SI). Ti-Beta-N-S-72h and Ti-Beta-S-F-48h were substantially amorphous, while Ti-Beta-N-F-72h was fully crystalline. This reveals that the NMP and fluoride medium plays a synergistic role in shortening the crystallization time to 72 h, even if the seeds are crucial to further shorten it to 20 h (Ti-Beta-N-S-F-20h, Fig. 1). It is worth noting that in the presence of NMP, the effective OH^- concentration is partially reduced due to alkali-catalyzed ring-opening reactions with TEAOH, as also reported in the literature.[20] In our system, this decrease in alkalinity (thus in the mineralizing effect of OH^-) is not compensated by additional hydroxide, but instead by fluoride anions, which are well known to act as highly efficient mineralizing agents for BEA-type zeolites under lower-pH conditions. Therefore, addition of HF is essential in the present synthesis strategy. In control experiments, the synthesis of Ti-Beta using NMP and seeds (Ti-Beta-N-S-72h), in the absence of HF failed, yielding non-crystalline materials even with longer crystallization time (Fig. S1c). This observation confirms that, when NMP lowers the effective hydroxide concentration, fluoride ions are required to sustain the mineralization process and enable BEA crystallization.

Based on the evolution of crystallinity across the series, the samples selected for detailed characterization are Ti-Beta-N-S-F-20h, 48h, and 72h, Ti-Beta-N-F-72h, and Ti-Beta-F-336h (used as a reference material).

Information about the complex intergrowth of Beta polymorphs (A, B, and C) can be obtained from the shoulder observed at ~7.6° in the XRD patterns, since different stacking sequences generate differently shaped broad reflections.[9,26] The

intensity and sharpness of this shoulder are strongly influenced by the synthesis conditions, since the use of fluoride media generally promotes larger, better-ordered crystals with fewer connectivity defects,[27,28] while the basic (OH^-) route typically produces smaller crystals with higher defectivity, leading to broader and less resolved features, as in the case of Beta-N-24h (Fig. S1). In the present case, although the main synthesis was carried out in the HF medium (Ti-Beta-F-336h and Ti-Beta-N-F series), the use of seeds, previously synthesized under OH^- conditions, partially transferred their structural disorder into the crystallization process, resulting in a noticeable fading of the 7.6° shoulder in seeded samples (Ti-Beta-N-S-F series, Fig. 1a) compared to the unseeded HF syntheses (Ti-Beta-F-336h and Ti-Beta-N-F series, Fig. 1b).

To evaluate whether the timing of NMP addition influences the crystallization of Ti-Beta, a series of control experiments were conducted where NMP was introduced at different stages of the synthesis process (Fig. S1). The results indicate that delayed introduction of NMP during the synthesis may lead to incomplete crystallization.

The morphology of the Ti-Beta crystals was analysed by FESEM for representative samples, Ti-Beta-F-336h, Ti-Beta-N-F-72h, and Ti-Beta-N-S-F-20h, revealing a clear influence of seeding on the crystal size and uniformity (Fig. 2). The samples synthesized using both NMP and seeds exhibited uniform crystals with significantly smaller dimensions compared to the unseeded counterparts. This is attributed to the high nucleation density provided by the surface of the dealuminated nano-seed crystals (Fig. S2 and S3 and Table S1), which restricted individual crystal growth and promoted the formation of smaller, more uniform particles. In comparison, the sample synthesized with just NMP showed larger well-faceted crystallites, indicative of slower nucleation. These findings highlight the synergistic effect of NMP and seeds in directing fast and controlled crystallization of Ti-Beta under conventional HF conditions, within 20 h of crystallization time.

The textural properties of the synthesized Ti-Beta zeolites were investigated by N_2 adsorption–desorption measurements at −196 °C. All crystalline samples exhibited type Ia isotherms,[10] with a sharp uptake at low relative pressures ($p/p_0 < 0.1$), which is indicative of a predominantly ultramicroporous structure typical of zeolite Beta (Fig. 3). When a hysteresis loop is superimposed on a type I isotherm, it usually reflects textural or interfacial phenomena rather than simple micropore filling. In zeolites, such behaviour has been related to the existence of interparticle mesoporosity as well as to intergrowths or stacked layers that generate slit-like voids. In highly crystalline, well-intergrown domains, desorption can be hindered, leading to metastable adsorbate phases that appear as hysteresis despite the intrinsically microporous nature of the framework.[10,29–32] Moreover, TEA^+ cations compensate for framework silanol defects, and their concentration increases with the addition of NMP, thereby promoting higher densities of connectivity defects.[20] The SSA values and micropore volume of the samples are summarized in Table 2.

The pore size distribution of Ti-Beta samples shows a single family of pores at approximately 6.5 Å which is consistent with the ultramicropore dimensions of the Beta framework reported in the IZA structure database (Fig. 3b).[10,25,30,31] In addition, Beta-N-24h, displays two additional families of pores, which can be attributed to voids among nano-sized particles, generated during the OH-mediated synthesis route. Their contribution to

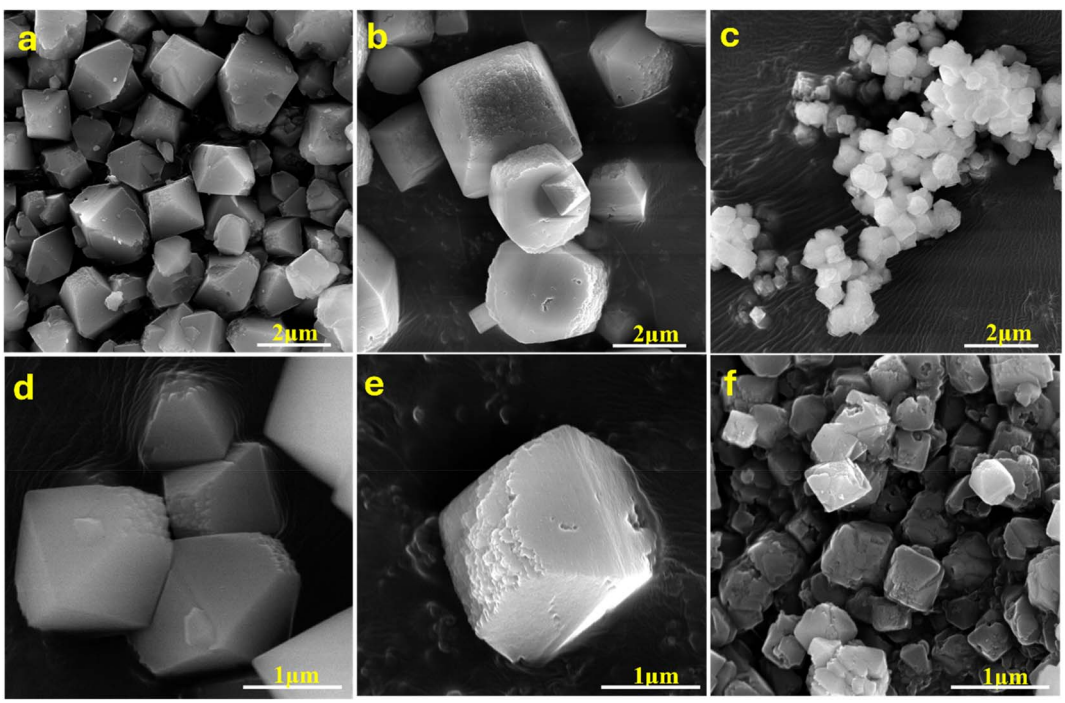

Fig. 2 SEM images of Ti-Beta samples: (a and d) Ti-Beta-F-336h, (b and e) Ti-Beta-N-F-72h, and (c and f) Ti-Beta-N-S-F-20h. (a–c) 300 00× magnification and (d–f) 800 00× magnification.

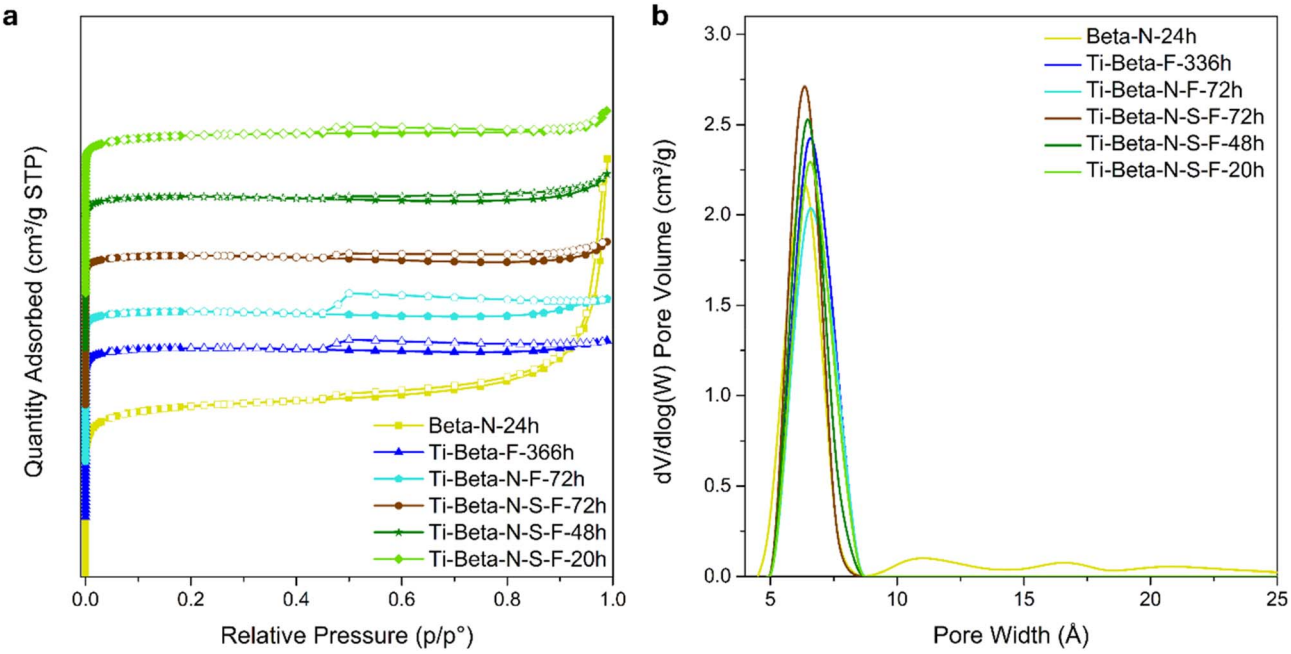

Fig. 3 (a) N_2 adsorption–desorption isotherms at −196 °C of the Ti-Beta samples, offset by 50 $cm^3\ g^{-1}$ STP for visual clarity, and (b) DFT-derived pore size distribution of the same samples.

the total pore volume is, however, very limited. The cumulative pore volume *vs.* pore width plot is shown in the Fig. S4 of the SI. A detailed comparison of S_{BET}, $S_{Langmuir}$, $S_{micropore}$, $S_{external}$, and micropore volumes derived from DFT and t-plot analyses is presented in the SI (Fig. S7), suggesting that the minor variation of surface-area-derived parameters can be related to the progressive improvement in Ti-Beta crystal quality as a consequence of the increase of the crystallization time.

UV-vis diffuse reflectance spectroscopy was employed to investigate the coordination environment and dispersion of Ti in the synthesized Ti-Beta zeolites (Fig. 4a). The spectra of all the activated samples were dominated by an intense absorption band centred around 210–220 nm. This band is associated with a $O^{2-} \rightarrow Ti^{4+}$ metal to ligand charge transfer (LMCT) transition, which is a well-established marker of tetrahedral framework-substituted Ti(IV) species in zeolites.[33–37] A minor shoulder was observed in the 250–270 nm region for some samples, particularly in Ti-Beta-N-S-F-48h, Ti-Beta-N-S-F-72h, and Ti-Beta-F-336h, which may be attributed to the presence of a small amount of extra-framework Ti.[35,36] These samples also show a weak tail above 300 nm, suggesting that a fraction of Ti may have segregated as TiO_2, whereas it is not observed in the Ti-Beta-N-S-F-20h sample (where only the tetrahedral Ti component is present). Hence upon reducing the crystallization time from 72 to 20 h in the Ti-Beta-N-S-F series, the Ti insertion in framework positions is favoured and the formation of extra-framework Ti species is avoided. These results reinforce the conclusion that the combined use of NMP and seeds allows both accelerated crystallization and effective incorporation of Ti(IV) into the zeolite framework, resulting in a particularly narrow Ti speciation for the short crystallization time. As supplementary information, the spectra of the samples recorded on pristine (*i.e.*, not thermally dehydrated) samples are shown in Fig. S8.

Table 2 Textural properties of Ti-Beta samples

			SSA ($m^2\ g^{-1}$)		Pore volume ($cm^3\ g^{-1}$)		
Sample	Ti/Si molar ratio[a]	TiO_2 wt%[a]	S_{BET}[b]	$S_{Langmuir}$[c]	V_{total}	V_{micro}[d]	V_{meso}[e]
Beta-N-24h	—	—	596.6 ± 0.7	681.3 ± 1.2	0.286	0.283	0.003
Ti-Beta-F-336h	0.017	2.27	630.0 ± 0.7	675.0 ± 0.1	0.298	0.298	0
Ti-Beta-N-F-72h	0.006	0.84	561.0 ± 0.7	597.0 ± 0.4	0.263	0.263	0
Ti-Beta-N-S-F-72h	0.015	2.00	561.2 ± 0.7	597.7 ± 0.3	0.280	0.280	0
Ti-Beta-N-S-F-48h	0.026	3.44	571.5 ± 0.5	609.2 ± 0.5	0.277	0.277	0
Ti-Beta-N-S-F-20h	0.014	1.89	578.6 ± 0.3	636.2 ± 0.6	0.273	0.273	0
Ti-Beta-N-S-F-14h[f]	0.01	1.28	—	—	—	—	—

[a] Determined by EDX measurements. [b] BET range = 0.008–0.040 (p/p_0). [c] Langmuir range = 8–18 (kPa), the BET and Langmuir linear fitting plots are shown in Fig. S5 and S6. [d] Calculated from the cumulative pore volume plot for micropores with a size <20 Å. [e] $V_{meso} = V_{total} - V_{micro}$. [f] N_2 adsorption–desorption measurements have not been performed on Ti-Beta-N-S-F-14h due to its partial crystallinity.

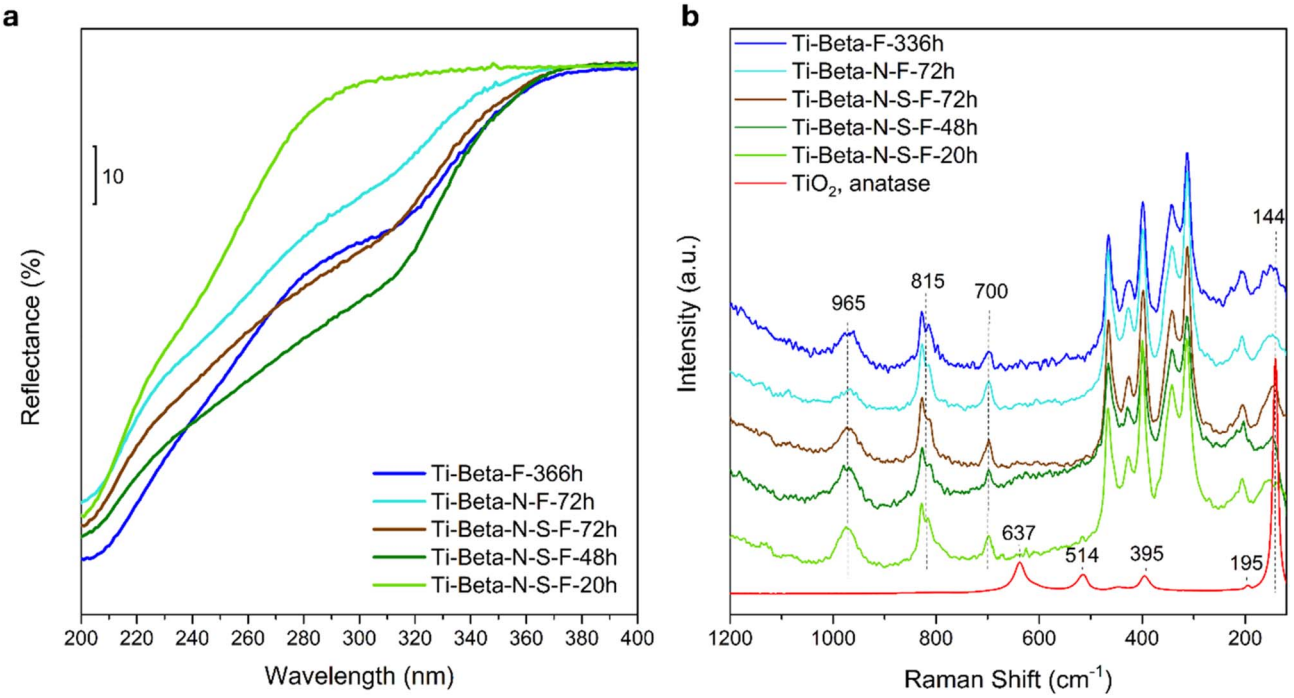

Fig. 4 (a) UV-vis spectra of activated Ti-Beta samples, (b) Raman spectra of Ti-Beta samples, collected with a 785 nm laser, in comparison to anatase TiO_2. Raman spectra are normalized to their maximum intensity and vertically shifted for visual clarity.

Raman spectroscopy (785 nm laser) was used to further probe the local coordination of Ti species in the synthesized Ti-Beta zeolites and to detect any traces of crystalline anatase TiO_2 (Fig. 4b). Bands in the range of 300–500 cm^{-1} and at 815 cm^{-1}, present in all the samples, are associated with Beta framework vibrations. The band at around 960 cm^{-1} is assigned to the Si–O–Ti stretching vibration of framework-incorporated Ti.[33–41] A weak signal is sometimes observed at ~700 cm^{-1} in Ti-containing zeolites, and in the case of TS-1, it has been assigned to isolated octahedral Ti species.[39,40,42] In our Ti-Beta samples, however, complementary characterization provides only negligible traces of extra-framework Ti. The appearance of the ~700 cm^{-1} band is therefore more reasonably related to the framework vibrations. This interpretation is supported by the fact that the same band is present in the Al-Beta and dealuminated Beta materials that contain no Ti, where it has been associated with defect-induced Si–O stretching, (Fig. S9).[2,41] Thus, in Ti-Beta, the ~700 cm^{-1} band should be interpreted as arising from defect-related or polymorph-dependent framework vibrations, rather than extra-framework Ti species. Additionally, bands diagnostic of TiO_2 (anatase polymorph) are expected at 144, 195, 395, 514, and 637 cm^{-1}, with the 144 cm^{-1} E_g mode being the most intense and easily detectable.[43] Among all the samples studied, the Raman signal at 144 cm^{-1} remains quite weak or even absent, suggesting that Ti remains largely well dispersed and incorporated into the zeolite framework and that possible TiO_2 clusters are extremely small and/or poorly crystalline.

IR spectroscopy in ATR mode was used to probe the framework vibrations and confirm the incorporation of Ti into the silica lattice of Ti-Beta zeolites (Fig. 5a and b). All crystalline samples exhibited the typical absorption bands of the zeolite frameworks: broad asymmetric stretching vibrations of Si–O–Si near 1100–1000 cm^{-1}, symmetric stretching at around 800 cm^{-1}, and bending modes near 460 cm^{-1}.[39] The bands in the 650–500 cm^{-1} range are instead typical of the Beta framework and they grow in the series upon increasing crystallization time, coherently with the XRD results (Fig. 5a).

In Ti-containing zeolites, the IR band at 960 cm^{-1} observed in activated samples (Fig. 5b) is widely recognized as a fingerprint of framework Ti species, but its shape differs among frameworks. In TS-1 (MFI), although there are 12 distinct crystallographic T-sites, Ti tends to occupy a narrower subset, and the resulting 960 cm^{-1} absorption is relatively sharp and symmetric. In contrast, Beta zeolites possess 9 non-equivalent T-sites, and Ti incorporation across these environments perturbs the Si–O–Ti linkages differently, producing a broadened band often accompanied by discernible shoulders (highlighted in the inset of Fig. 5b at 970, 957 and 943 cm^{-1}).[33,39,41,44] These spectral features reflect the coexistence of slightly shifted Si–O vibrations arising from Ti atoms accommodated in multiple crystallographic sites. Theoretical and spectroscopic studies by Bordiga and co-workers[39,41] demonstrated that the 960 cm^{-1} vibration should be understood as a collective mode of coupled Si–O oscillators perturbed either by Ti substitution or by structural defects such as silanols. These contributions can overlap, making the band sensitive to both Ti framework incorporation and defectivity. Consequently, while the band in TS-1 is sharper and better correlated with Ti content, in Ti-Beta its broadened, shoulder-rich profile serves as a sensitive

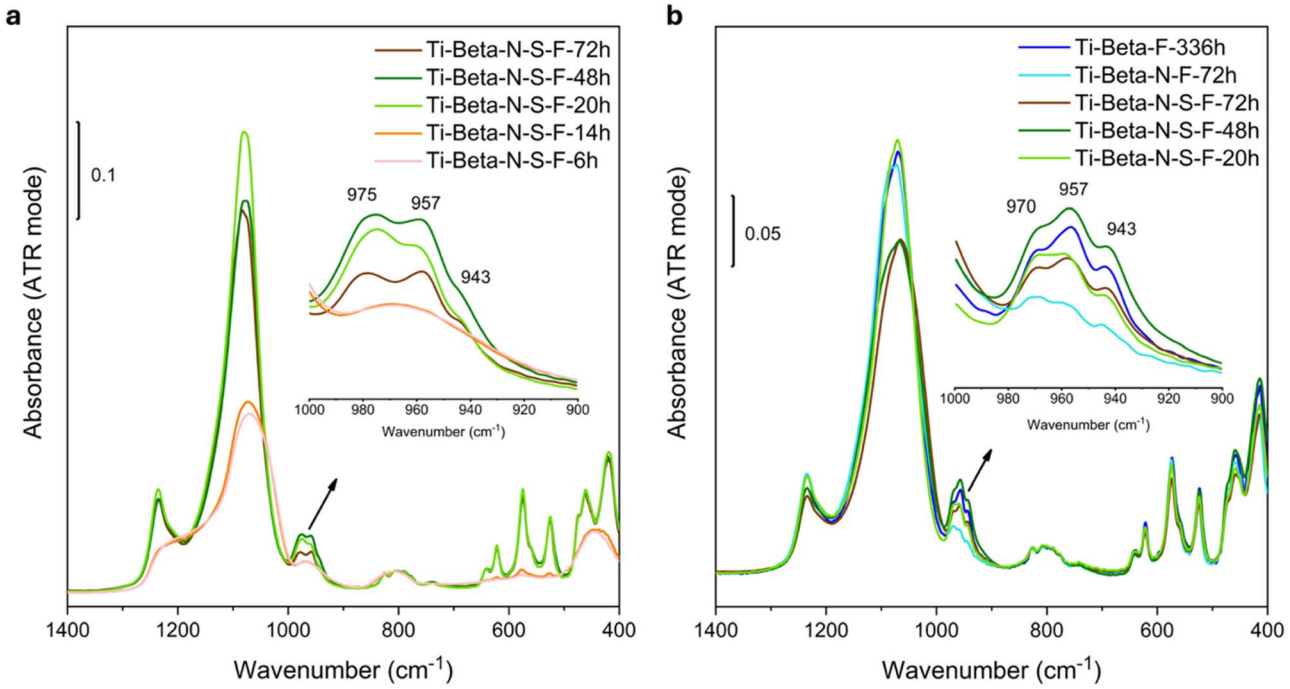

Fig. 5 (a) ATR-IR spectra of non-activated Ti-Beta-N-S-F samples and (b) IR spectra of activated Ti-Beta samples. All the spectra were normalized to their 800 cm^{-1} signals.

indicator of site heterogeneity and defect coupling within the framework.[30,38,41,42,44–46] Moreover, the relative intensities of these bands varied among the present samples, suggesting differences in Ti dispersion and coordination.

Crystallinity and framework Ti evolution of the Ti-Beta-N-S-F series

The evolution of structural and spectroscopic features in the Ti-Beta samples synthesized with seeds and NMP highlights a clear time-dependent balance between crystallinity and Ti site coordination. Fig. 6 shows the Ti/Si molar ratio, the integrated area of the 960 cm^{-1} band (normalized to TiO_2 wt% amount based on EDX results), the Kubelka–Munk (K–M) intensity (calculated by converting the reflectance at 270 and 320 nm by applying the Kubelka–Munk function, and further normalizing to TiO_2 wt%) and the apparent degree of crystallinity (calculated based on the sum of the integrated areas in the 5°–10° and 21°–24° 2θ regions of the XRD patterns and considering Ti-Beta-N-S-F-48h as the 100% crystallinity reference).

After only 20 h, the sample displays an apparent crystallinity of 95%, a Ti/Si of 0.0142, a strong 960 cm^{-1} IR band (Fig. 5b) and the lowest extra-framework Ti intensity in the optical spectrum. This suggests that after 20 h the Ti is totally inserted into framework positions. Extending the crystallization time to 48 h results in the highest XRD crystallinity (100%) and highest Ti/Si (0.026). The 960 cm^{-1} band (Fig. 5b) is the most intense among the series, but the integrated area of the 960 cm^{-1} band normalized to TiO_2 wt% decreases and the optical absorbance associated with extra-framework Ti increases compared to the sample at 20 h. This suggests that the remaining Ti is only partially inserted into the framework and it is present as extra-framework Ti species as well. At 72 h, a negligible decline in apparent crystallinity by XRD was observed (crystallinity = 98%), together with a decrease of the total Ti content (Ti/Si = 0.015). The 960 cm^{-1} IR band (Fig. 5b) shows nearly the same perfect Ti concentration as that of the 20 h sample. However, the normalized K–M intensity slightly decreases and the IR band at ~960 cm^{-1} increases relative to the 48 h sample. This result indicates that the framework Ti species are partially solubilized under reaction conditions for prolonged time. The extra-framework Ti are solubilized as well but resulting in an increased amount of extra-framework species compared to the 20 h sample, given nearly the same Ti/Si. We can tentatively attribute this to dissolution–recrystallization, which could be explained by considering that extra-framework species are more stable under basic conditions due to their aggregation than the zeolite itself.[47]

Overall, the Ti-Beta-N-S-F-20h sample represents the most efficient compromise between crystallinity, framework Ti incorporation, and synthesis time, while Ti-Beta-N-S-F-48h marks a threshold where extra-framework Ti starts to accumulate (though crystallinity is improved).

Study of acidic Ti-sites using acetonitrile as a probe molecule

In Ti-containing Beta zeolites, the potential acidic functionalities can be broadly classified as (i) framework Ti(IV) sites in tetrahedral coordination, which behave as Lewis acid centres, and (ii) hydroxyl groups, including silanols (Si–OH) and defect-related Ti–OH species, which act as weak Brønsted acid sites.[39,48] IR spectroscopy, along with basic probe molecules, is a widely adopted approach to characterize the nature, strength, and accessibility of these sites,[39,41,48–52] since their properties are

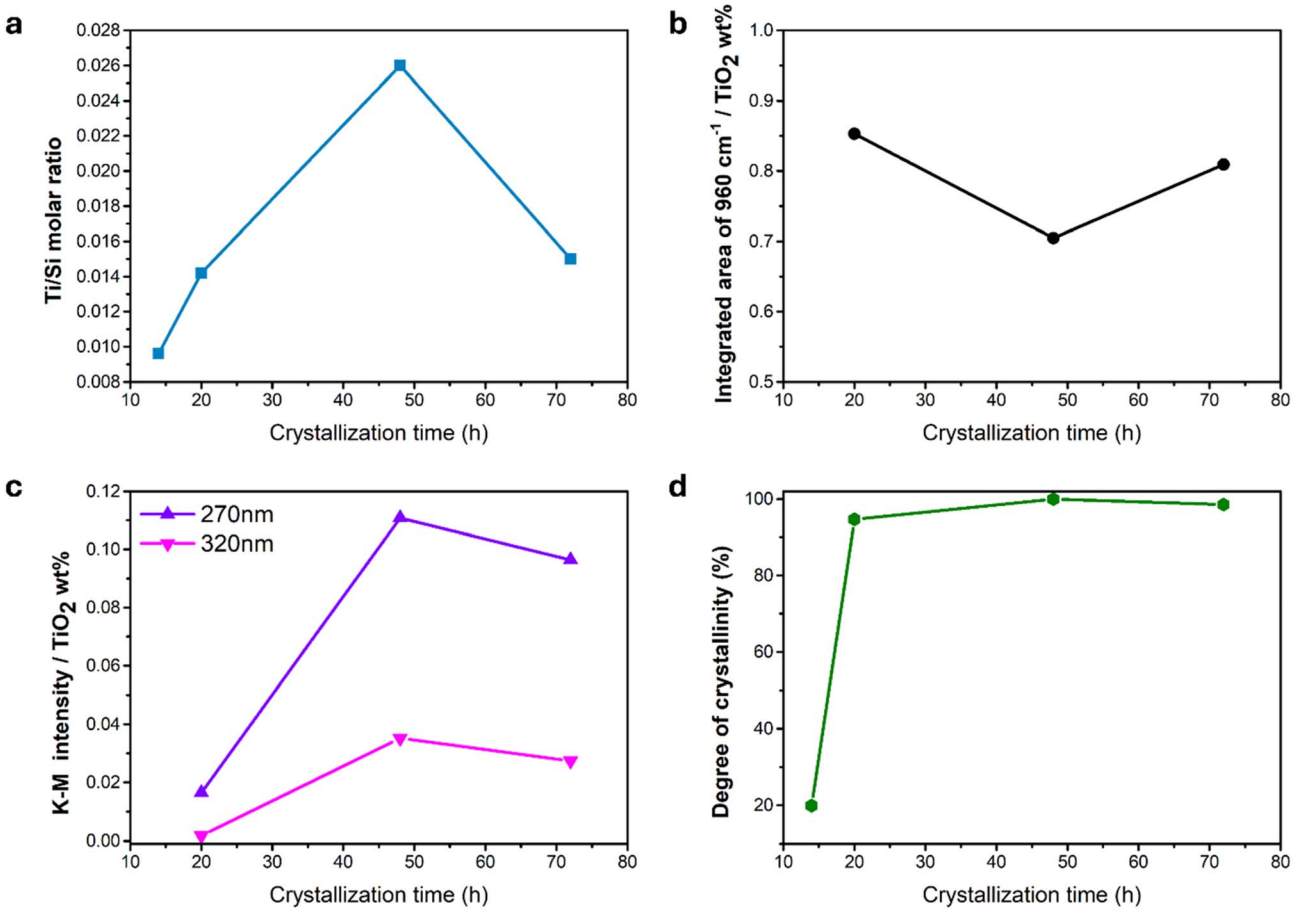

Fig. 6 Evolution of structural and spectroscopic features in the Ti-Beta-N-S-F series. (a) Ti/Si molar ratio based on the EDX analysis, (b) integrated area of the 960 cm^{-1} band in the range of 900–1000 cm^{-1} range, (c) Kubelka–Munk intensity of the bands at 270 and 320 nm. Both panels (b and c) are normalized to the TiO_2 content (wt%) derived from the EDX analysis. (d) Degree of crystallinity of the samples estimated from the XRD patterns, based on summing the integrated peaks areas in the 5–10 and 21–24 2θ ranges and considering Ti-Beta-N-S-F-48h as the 100% crystallinity reference.

closely related to catalytic behaviour and the formation of undesired by-products. IR spectroscopy with deuterated acetonitrile as a probe molecule was employed to investigate the Lewis acidity of Ti(IV) sites of the Ti-Beta-N-S-F-20h sample and to assess the hydroxyl population (Fig. 7a and b). Upon CD_3CN adsorption, the consumption of hydroxyl groups is evidenced by the decrease in bands above 3600 cm^{-1}, corresponding to external, internal, and terminal silanols,[51,52] together with the concomitant appearance of a broad absorption centred at around 3400 cm^{-1}, indicative of hydrogen-bonded adducts between silanol groups and CD_3CN. In the ν(CN) stretching region, three components can be distinguished: (i) liquid-like physisorbed CD_3CN at ~2263 cm^{-1}, (ii) CD_3CN interacting with hydroxyl groups at ~2275 cm^{-1}, and (iii) CD_3CN coordinated to Ti(IV) Lewis sites in tetrahedral framework positions at ~2308 cm^{-1}.[48–52] The ~2308 cm^{-1} band represents a +45 cm^{-1} shift compared to the physisorbed ν(CN) frequency, testifying to the Lewis acidity of framework Ti(IV) centres in Beta. This shift is comparable to the values reported for TS-1 (+37 cm^{-1}), Ti-MWW (+43 cm^{-1}) and slightly lower than those observed for Al(III) Lewis sites in ZSM-5 (+50 cm^{-1}), suggesting that the Ti(IV) sites in Beta exhibit medium Lewis acid strength.[41,51] This observation is consistent with the reversible coordination of CD_3CN to Ti(IV) sites. After outgassing, the ν(CN) band associated with Ti(IV) returns to the baseline, and the hydroxyl-related features reappear, confirming the complete reversibility of the interaction.

Exploring the interaction of titanium active sites with H_2O_2

As a further probe of the accessibility and potential reactivity of Ti-Beta presented in this work, we investigated the formation of Ti-(hydro)peroxo complexes by means of DR-UV-vis spectroscopy, as depicted in Fig. 8. The UV-vis spectrum of the pristine Ti-Beta-N-S-F-20h sample exhibits the expected band at ~220 nm, typical of isolated framework Ti(IV) (see also Fig. 4a and related comment).[39,40,42] Upon incipient impregnation of the sample with a 30 wt% aqueous solution of H_2O_2, a new shoulder in the 350–500 nm range appears in the UV-vis spectrum, which is ascribed to the formation of Ti–(hydro)peroxo complexes.[39,41,44,52] These arise from coordination of H_2O_2 to framework Ti sites, either through a side-on peroxo (pale-yellow colour) adduct or *via* proton transfer to yield Ti-hydroperoxo

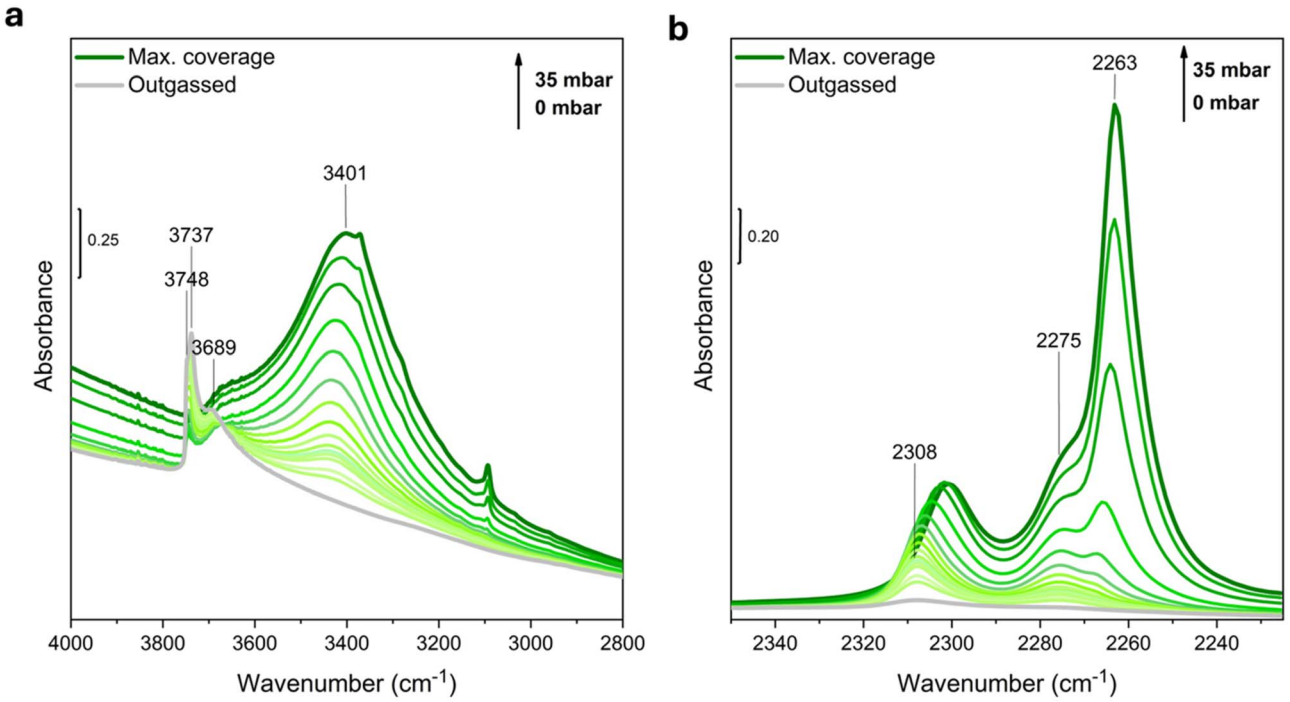

Fig. 7 IR spectra in different spectral ranges of activated Ti-Beta-N-S-F after contact with CD_3CN at room temperature (RT), recorded in transmission mode. (a) OH-stretching region and (b) CN-stretching region. The spectrum of the activated sample was subtracted as the baseline. All the spectra were normalized to the overtone bands at 1988 cm^{-1} of the activated sample and vertically shifted for clear visualization.

species (uncoloured).[42] These species are connected by an equilibrium driven by the overall sample hydration, being the Ti-peroxo complex progressively converted into Ti-hydroperoxo upon drying. The latter is quite stable and can be effectively re-converted to the Ti-peroxo form by rehydrating the sample with pure H_2O. A further 24 h dehydration reverts the equilibrium, showing the cyclability of the process.[41,45] Furthermore, the stability of Ti-Beta-N-S-F-20h after H_2O_2 exposure was examined through complementary characterization, aimed at detecting possible Ti leaching and framework degradation. The results of these analyses, provided in the SI (Fig. S10–13 and Table S2), show that no significant alteration of Ti amount, speciation and framework crystallinity is observed under the considered exposure conditions.

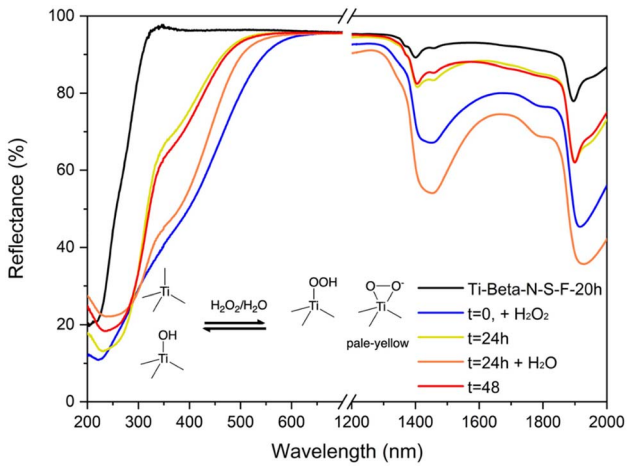

Fig. 8 UV-vis spectra in DR mode of not activated Ti-Beta-N-S-F-20h under different conditions, black: the spectrum of the sample in air, indicating the Ti(IV) band at ~220. Blue: collected immediately after the addition of H_2O_2 (time = 0). Yellow: the spectrum after 24 h of drying at room temperature. Orange: the spectrum upon addition of H_2O (time = 24 h). Red: the spectrum after 48 h following H_2O_2 addition and subsequent drying at room temperature.

Conclusions

In this work, we demonstrated an accelerated route for the synthesis of framework Ti-substituted Beta zeolites by employing *N*-methyl-2-pyrrolidone (NMP) as a crystallization promoter, either alone or in combination with seeds. Dealuminated Beta seeds act as classical crystallization promoters that lower the nucleation barrier and accelerate crystal growth by providing pre-formed structural units or a crystalline surface where secondary nucleation occurs. In contrast, NMP does not serve as a structural promoter, but, under basic hydrothermal conditions, it suppresses Hofmann degradation of TEAOH, preserving the effective TEA^+ concentration and stabilizing the gel chemistry. This is further confirmed by the absence of clear signatures in TGA profiles and ATR-IR spectra of the as-synthesized (*i.e.* non-calcined) samples, as detailed in Fig. S14 of the SI.

Compared to conventional methods, the presence of NMP significantly reduced the crystallization time, with a fully crystalline Ti-Beta obtained within 72 h, while the synergistic use of NMP and seeds further shortened the process to only 20 h. Overall, the accelerated crystallization achieved through the use

of NMP in combination with seeding, not only reduced the synthesis time of Ti-Beta to 20 h, but also proved crucial in preserving the Ti speciation within the zeolite framework. The short crystallization time effectively limited the migration and/or segregation of Ti species, promoting their incorporation into tetrahedral framework positions rather than forming extra-framework TiO_2. However, this beneficial effect gradually diminished as the crystallization time increased to 48 h and 72 h, when partial rearrangement and migration of Ti species likely occurred, leading to a reduced fraction of framework-coordinated Ti with respect to extra-framework Ti/TiO_2. This finding underscores the critical role of kinetic control during zeolite crystallization, showing that here a rapid synthetic method is not only beneficial for efficiency, but also essential for stabilizing the desired Ti environment. Such framework Ti is furthermore accessible and available as a potential catalytic centre in the presence of H_2O_2, also featuring good stability upon prolonged exposure to the reagent.

Overall, this study provides new insight into the role of NMP as a multifunctional additive in zeolite synthesis, not only accelerating crystallization but also promoting efficient framework Ti incorporation. The methodology establishes a versatile and time-efficient route to prepare Ti-Beta zeolites with features that make them suitable for future catalytic studies, opening the way to broader applications of large-pore Ti-zeolites in selective oxidation reactions of bulky substrates.

Author contributions

Hedieh Tabatabaeizadeh carried out the synthesis of all materials, performed the experiments, analyzed and interpreted the data, and wrote the original draft of the manuscript. Francesca Rosso contributed to conceptualization, supervision, writing – review and editing. Francesca Bonino contributed to conceptualization, writing – review and editing. Silvia Bordiga contributed to conceptualization, funding acquisition, resources, writing – review and editing. Miguel A. Camblor contributed to conceptualization, funding acquisition, resources, supervision, writing – review and editing. Matteo Signorile and Valentina Crocellà contributed to conceptualization, funding acquisition, project administration, resources, supervision, writing – review and editing. All authors approved the final version of the manuscript.

Conflicts of interest

There are no conflicts to declare.

Data availability

Data for this paper are available at Zenodo at https://doi.org/10.5281/zenodo.18693012. Supplementary information: additional XRD patterns, SEM images, BET and Langmuir linear fitting plots, UV-visible spectra for pristine samples, Raman spectra of Beta-N-24h and deAl-Beta-N-24h, ATR and TGA analyses for the presence of NMP in the Ti-Beta samples and different characterization methods for the assessment of Ti leaching and framework integrity after the H_2O_2 treatment. See DOI: https://doi.org/10.1039/d6ta00222f.

Ref. 4, 8, 11, 19, 34, 39, 40, 43, 52 are also cited in the Supplementary information (SI).

Acknowledgements

The authors have received funding from the Project CH4.0 under the MUR program "Dipartimenti di Eccellenza 2023–2027" (CUP: D13 C22003520001). Additional funding from the Spanish Ministry of Science and Innovation (PID2022-137889OB-I00 and MCIN/AEI/10.13039/501100011033) is gratefully acknowledged. F.R. acknowledges the project CUPId, "Catalytic Upcycling of PolyolefIn waste: a matter of awareness" under the MUR program PRIN2022 (cod.: 2022PPXWMS and CUP: D53D23009210006) for financial support. The authors acknowledge Dr Maria Carmen Valsania for the SEM-EDX elemental analysis and for fruitful discussion.

References

1 B. Wang, H. Han, B. Ge, J. Ma, J. Zhu and S. Chen, *New J. Chem.*, 2019, **43**, 10390–10397.
2 M. Signorile, V. Crocellà, A. Damin, B. Rossi, C. Lamberti, F. Bonino and S. Bordiga, *J. Phys. Chem. C*, 2018, **122**, 9021–9034.
3 P. Tao, X. Wang, Q. Zhao, H. Guo, L. Liu, X. Qi and W. Cui, *Appl. Catal., B*, 2023, **325**, 122392.
4 H. Pan, R. Peng, Z. Zhu, H. Xu, M. He and P. Wu, *Catalysts*, 2022, **12**, 434.
5 N. Hoeven, G. Mali, M. Mertens and P. Cool, *Microporous Mesoporous Mater.*, 2019, **288**, 109588.
6 G. Yang, Z. Qiu, S. Peng, M. Nan, L. Li, Y. Hou and X. Chen, *Inorg. Chem.*, 2022, **61**, 4887–4894.
7 M. A. Camblor, A. Mifsud and J. Pérez-Pariente, *Zeolites*, 1991, **11**, 792–797.
8 X. Deng, Y. Xu, J. Liu, D. Lin, Z. Zong, J. Yuan, Z. Li, G. Zhao, Y. Zhang, Y. Liu, X. Chen, X. Feng, D. Chen, C. Yang and H. Shan, *Ind. Eng. Chem. Res.*, 2024, **63**, 3817–3826.
9 J. M. Newsam, M. M. J. Treacy, W. T. Koetsier and C. B. De Gruyter, in *Zeolites: Facts, Figures, Future*, ed. H. van Bekkum, E. M. Flanigen and J. C. Jansen, Elsevier, Amsterdam, 1989, vol. 49, pp. 467–479.
10 M. Thommes, K. Kaneko, A. V. Neimark, J. P. Olivier, F. Rodriguez-Reinoso, J. Rouquerol and K. S. Sing, *Pure Appl. Chem.*, 2015, **87**, 1051–1069.
11 Z. Liu, L. Zhao, T. Zhang, Y. Wang, Y. Xu, S. Komarneni, Y. Wang, X. Liu and Z. Yan, *J. Porous Mater.*, 2019, **26**, 1017–1025.
12 J. M. Thomas, R. Raja and D. W. Lewis, *Angew. Chem., Int. Ed.*, 2005, **44**, 6456–6482.
13 J. B. Nagy, R. Aiello, G. Giordano, A. Katović, F. Testa, Z. Kónya and I. Kiricsi, in *Molecular Sieves – Science and Technology, Vol. 5: Characterization II*, ed. H. G. Karge and J. Weitkamp, Springer-Verlag, Berlin/Heidelberg, 2006, pp. 365–478.

14 F. Dubray, PhD thesis, Normandie Université, 2020, https://theses.hal.science/tel-03510144/, (accessed December 2025).
15 R. Aiello, J. B. Nagy, G. Giordano, A. Katović and F. Testa, *C. R. Chim.*, 2005, **8**, 321–329.
16 J. Pérez-Ramírez and M. Sánchez-Sánchez (ed.), *Structure and Reactivity of Metals in Zeolite Materials*, Springer International Publishing, Cham, 2018.
17 L. Hong, J. Zang, B. Li, G. Liu, Y. Wang and L. Wu, *Inorganics*, 2023, **11**, 214.
18 D. Zhao, X. Li, W. Chu, Y. Wang, W. Xin, C. Feng, G. Hou, L. Xu, S. Liu and X. Zhu, *Microporous Mesoporous Mater.*, 2023, **347**, 112342.
19 C. Yang, D. Zhao, W. Chu, Y. Wang, X. Li, S. Xie, W. Xin, X. Zhu, S. Liu and L. Xu, *J. Mater. Chem. A*, 2020, **8**, 26139–26149.
20 D. Zhao, W. Chu, Y. Wang, X. Zhu, X. Li, S. Xie, J. An, W. Xin, S. Liu and L. Xu, *J. Mater. Chem. A*, 2018, **6**, 24614–24624.
21 X. Wang, D. Zhao, W. Chu, C. Yang, Y. Wang, X. Zhu, W. Xin, Z. Liu, H. Wang, S. Liu and L. Xu, *Microporous Mesoporous Mater.*, 2020, **294**, 109944.
22 J. Li, H. Liu, T. An, Y. Yue and X. Bao, *RSC Adv.*, 2017, **7**, 33714–33725.
23 T. Blasco, M. A. Camblor, A. Corma, P. Esteve, A. Martinez, C. Prieto and S. Valencia, *Chem. Commun.*, 1996, 2367–2368.
24 J. Rouquerol, P. Llewellyn and F. Rouquerol, in *Characterization of Porous Solids VII*, ed. P. Llewellyn, F. Rodriguez-Reinoso, J. Rouquerol and N. Seaton, Elsevier, Amsterdam and Oxford, 2007, pp. 49–56.
25 *International Zeolite Association*, https://www.iza-online.org, (accessed November 24, 2025).
26 J. B. Higgins, R. B. LaPierre, J. L. Schlenker, A. C. Rohrman, J. D. Wood, G. T. Kerr and W. J. Rohrbaugh, *Zeolites*, 1988, **8**, 446–452.
27 M. A. Camblor, A. Corma and S. Valencia, *J. Mater. Chem.*, 1998, **8**, 2137–2145.
28 A. Corma, V. Fornes, S. B. Pergher, Th. L. M. Maesen and J. G. Buglass, *Nature*, 1998, **396**, 353–356.
29 X. Li and S. Li, *Arab. J. Chem.*, 2025, **18**, 1902024.
30 M. Moliner and A. Corma, *Microporous Mesoporous Mater.*, 2014, **189**, 31–40.
31 A. Petushkov, G. Merilis and S. C. Larsen, *Microporous Mesoporous Mater.*, 2011, **143**, 97–103.
32 A. Song, J. Ma, D. Xu and R. Li, *Catalysts*, 2015, **5**, 2098–2114.
33 M. A. Camblor, A. Corma and J. Pérez-Pariente, *J. Chem. Soc., Chem. Commun.*, 1993, 557–559.
34 F. Rosso, A. Rizzetto, A. Airi, K. Khoma, M. Signorile, V. Crocellà, S. Bordiga, S. Galliano, C. Barolo, E. Alladio and F. Bonino, Rationalization of TS-1 Synthesis through the Design of Experiments, *Inorg. Chem. Front.*, 2022, **9**, 3372–3383.
35 M. Signorile, L. Braglia, V. Crocellà, P. Torelli, E. Groppo, G. Ricchiardi, S. Bordiga and F. Bonino, *Angew. Chem., Int. Ed.*, 2020, **59**, 18145–18150.
36 Q. Guo, K. Sun, Z. Feng, G. Li, M. Guo, F. Fan and C. Li, *Chem.–Eur. J.*, 2012, **18**, 13854–13860.
37 D. Scarano, A. Zecchina, S. Bordiga, F. Geobaldo, G. Spoto, G. Petrini, G. Leofanti, M. Padovan and G. Tozzola, *J. Chem. Soc., Faraday Trans.*, 1993, **89**, 4123–4130.
38 G. Xiong, Y. Cao, Z. Guo, Q. Jia, F. Tian and L. Liu, *Phys. Chem. Chem. Phys.*, 2016, **18**, 190–196.
39 S. Bordiga, C. Lamberti, F. Bonino, A. Travert and F. Thibault-Starzyk, *Chem. Soc. Rev.*, 2015, **44**, 7262–7341.
40 X. Liang, X. Peng, C. Xia, H. Yuan, K. Zou, K. Huang, M. Lin, B. Zhu, Y. Luo and X. Shu, *Ind. Eng. Chem. Res.*, 2021, **60**, 1219–1230.
41 G. Ricchiardi, A. Damin, S. Bordiga, C. Lamberti, G. Spanò, F. Rivetti and A. Zecchina, *J. Am. Chem. Soc.*, 2001, **123**, 11409–11419.
42 B. Wang, Y. Guo, J. Zhu, J. Ma and Q. Qin, *Coord. Chem. Rev.*, 2023, **476**, 214931.
43 S. Challagulla, K. Tarafder, R. Ganesan and S. Roy, *Sci. Rep.*, 2017, **7**, 8783.
44 S. Klinyod, K. Yomthong, D. Suttipat, P. Pornsetmetakul, P. Kidkhunthod, K. Choojun, S. Namuangruk, T. Sooknoi and C. Wattanakit, *ChemCatChem*, 2025, **17**, 202401862.
45 F. Bonino, A. Damin, G. Ricchiardi, M. Ricci, G. Spanò, R. D'Aloisio, A. Zecchina, C. Lamberti, C. Prestipino and S. Bordiga, *J. Phys. Chem. B*, 2004, **108**, 3573–3583.
46 A. Petushkov, G. Merilis and S. C. Larsen, *Microporous Mesoporous Mater.*, 2011, **143**, 97–103.
47 R. Simancas, A. Chokkalingam, S. P. Elangovan, Z. Liu, T. Sano, K. Iyoki, T. Wakihara and T. Okubo, *Chem. Sci.*, 2021, **12**, 7677–7695.
48 C. Lamberti, A. Zecchina, E. Groppo and S. Bordiga, *Chem. Soc. Rev.*, 2010, **39**, 4951–5001.
49 R. Otomo, T. Nakamura and Y. Kamiya, *Microporous Mesoporous Mater.*, 2024, **378**, 113246.
50 E. L. Meijer, R. A. van Santen and A. P. J. Jansen, *J. Phys. Chem. A*, 1999, **103**, 2553–2560.
51 A. Zachariou, A. P. Hawkins, R. F. Howe, J. M. S. Skakle, N. Barrow, P. Collier, D. W. Nye, R. I. Smith, G. B. G. Stenning, S. F. Parker and D. Lennon, *ACS Phys. Chem. Au*, 2023, **3**, 74–83.
52 F. Rosso, A. Airi, M. Signorile, E. Dib, S. Bordiga, V. Crocellà, S. Mintova and F. Bonino, *Microporous Mesoporous Mater.*, 2024, **366**, 112924.